OCEANOGRAPHY

The 2022 Hunga-Tonga megatsunami: Near-field simulation of a once-in-a-century event

Sam J. Purkis[1,2]*, Steven N. Ward[3], Nathan M. Fitzpatrick[1], James B. Garvin[4], Dan Slayback[4], Shane J. Cronin[5], Monica Palaseanu-Lovejoy[6], Alexandra Dempsey[2]

Copyright © 2023 The Authors, some rights reserved; exclusive licensee American Association for the Advancement of Science. No claim to original U.S. Government Works. Distributed under a Creative Commons Attribution NonCommercial License 4.0 (CC BY-NC).

The Hunga Tonga–Hunga Ha'apai (HTHH) volcanic eruption in January 2022 generated catastrophic tsunami and contends for the largest natural explosion in more than a century. The main island, Tongatapu, suffered waves up to 17 m, and Tofua Island suffered waves up to 45 m, comfortably placing HTHH in the "megatsunami" league. We present a tsunami simulation of the Tongan Archipelago calibrated by field observations, drone, and satellite data. Our simulation emphasizes how the complex shallow bathymetry of the area acted as a low-velocity wave trap, capturing tsunami for more than 1 hour. Despite its size and long duration, few lives were lost. Simulation suggests that HTHH's location relative to urban centers saved Tonga from a worse outcome. Whereas 2022 seems to have been a lucky escape, other oceanic volcanoes have the capacity to spawn future tsunami at HTHH scale. Our simulation amplifies the state of understanding of volcanic explosion tsunami and provides a framework for assessment of future hazards.

INTRODUCTION

The Kingdom of Tonga comprises an archipelago of 169 islands situated at the northern end of the Tonga-Kermadec Arc (Fig. 1). As the Earth's fastest-converging, most seismically active subduction boundary, this arc has the highest known density of submarine volcanoes (*1*, *2*). Sedimentary evidence on the east (and possibly west) coast of the main island of Tongatapu document numerous tsunami events in prehistory and perhaps as recently as the mid-15th century CE (*3*, *4*), suggesting that large tsunami are not out of the ordinary. During an early 2015 eruption, the Hunga Tonga–Hunga Ha'apai (HTHH) submarine volcano (part of the 5-km-diameter submarine Hunga caldera) formed one of Earth's youngest volcanic islands (*5*, *6*). On 15 January 2022, the Hunga caldera explosively erupted at magnitudes far beyond the series of precursory Vulcanian or sub-Plinian eruptions that began on 20 December 2021. The 15 January eruption triggered shockwaves and pressure-coupled tsunami noticed as far away as the Caribbean. This event contends for the fiercest phreatoplinian volcanic eruption in more than a century, rivaling Krakatau in 1883, and displaying a VEI (volcanic explosivity index) = 6.3 (*7*, *8*).

We build forward from several recent studies that audit the atmospheric disturbances (*9*–*16*) and the pressure-coupled tsunami (*17*–*19*) induced by the explosion. Unlike these global-scale studies, we focus on the conventional tsunami generated by the explosive displacement of seawater, within the Tonga Archipelago where the impacts were most severe. By using the high-resolution shallow water bathymetry model of Purkis *et al.* (*20*), we are able to simulate the passage of the tsunami waveforms through the archipelago at much higher fidelity than previously achieved.

Combining pre- and post-satellite imagery (optical and radar), high-resolution digital elevation models (DEMs) with light detection and ranging (LIDAR), and on-site field and drone surveys, we have assembled 118 tsunami runup measurements for the 15 January 2022 HTHH explosive volcanic event spanning 10 islands of the Tonga Archipelago (Fig. 1). On the basis of Tsunami Squares simulations (*21*–*24*) and empirical pressure-distance-yield formulas derived from atomic bomb tests (*25*, *26*), all of these runup measurements can, to a reasonable extent, be fit by using an isotropic explosive source model consisting of one or more discrete explosions not exceeding 15 megatons (Mt). Ancillary information from barometer and tide records, ear- and eyewitnesses, video records, and well-documented data on pressure-related glass damage further constrains the time sequence and yields. We propose at least five blasts, two of relatively small size around 4:00 UTC (<0.1 Mt) and three increasingly larger ones at 4:06 (0.5 Mt), 4:18 (4 Mt), and 4:56 (15 Mt).

We consider our work to be of prescient value. First, it informs on the tsunami hazard posed by future eruptions of HTHH and other submarine volcanoes with shallow vents situated along oceanic arcs. Second, we contend that HTHH is an excellent natural laboratory to test hypotheses and models that can be deployed elsewhere to better understand similar eruptions and subsequent tsunami as preserved in the geologic record.

Diverse modes of volcanic tsunami

Many tsunami-generating mechanisms exist during volcanic activity (*3*, *27*), including explosions, pyroclastic and debris flows, earthquakes, flank and lava bench failures, caldera subsidence, and atmospheric waves. Unlike earthquake-induced tsunami, multiple tsunami can emanate from a single volcanic eruption, yielding waves of varied size, travelling at different velocities with different decay rates. Such diversity frustrates our current early warning systems and our modeling methods.

According to the simplest theory, a pressure front of the form $P(x\text{-}Vt)$ travelling at velocity V in a uniform ocean of depth H

[1]Department of Marine Geosciences, Rosenstiel School of Marine, Atmospheric, and Earth Science, University of Miami, Miami, FL, USA. [2]Khaled bin Sultan Living Oceans Foundation, Annapolis, MD, USA. [3]Institute of Geophysics and Planetary Physics, University of California Santa Cruz, Santa Cruz, CA, USA. [4]NASA Goddard Space Flight Center, Greenbelt, MD, USA. [5]School of Environment, The University of Auckland, Auckland, New Zealand. [6]U.S. Geological Survey, Reston, VA, USA.
*Corresponding author. Email: spurkis@earth.miami.edu

Downloaded from https://www.science.org on April 14, 2023

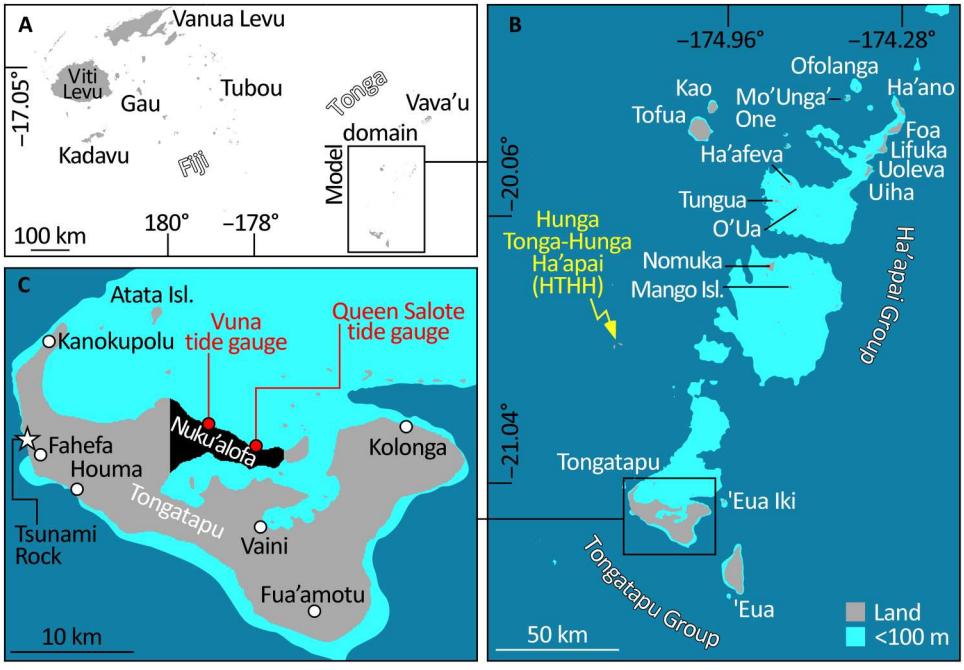

Fig. 1. The study area spans the southern portion of the Tonga Archipelago in the South Pacific. (**A**) Location of model domain. (**B**) The Tongatapu and Ha'apai island groups situate on a series of carbonate platforms mapped by the 100-m isobath (cyan polygons). The HTHH island and Hunga submarine caldera lies to the west of these platforms in deep water (yellow arrow). (**C**) Tongatapu is the main island of Tonga and the site of its capital, Nuku'alofa (city limits, black polygon). Here, tide gauges are stationed on the Queen Salote and Vuna Wharfs (red dots). The white star marks the position of Tsunami Rock, a 1600-ton erratic boulder in the vicinity of Fahefa village presumed deposited by prehistoric tsunami.

couples to a water wave $\eta(x,t)$ like

$$n(x,t) = \frac{P(x - Vt)}{\rho_w} \frac{H}{(V^2 - gH)} \quad (1)$$

You can see that the water wave motion follows the pressure history in shape and velocity but is scaled by a velocity differential. These are called pressure-coupled water waves. Equation 1 holds for both the direct blast waves and acoustic gravity (AG) waves despite the forms of the pressure front differing in size, shape, decay rate, velocity, and duration. The colossal HTHH detonation spawned at least two types of pressure-coupled tsunami, plus a conventional tsunami (*19*, *28*).

The first type of pressure-coupled tsunami emitted by HTHH was driven by the shockwave of the direct blast (*9*, *12*, *17*). Blast waves in the air are compression driven and expand at velocities slightly faster than the speed of sound (340 m/s). The blast-coupled water waves mimic the expanding blast front both in speed and shape. The expanding blast pressure decays at least as fast as distance$^{-3/2}$, so the blast-coupled water wave attenuates quickly. These types of waves are included in our simulation because they aid in constraining explosive yield, but they are relatively tiny at distance. For example, our overpressure model (Eq. 3) suggests that at 60-km distance, a 10 Mt blast (P = 0.3; psi = 2068 Pa) expanding over a 2000-m-deep ocean would couple to a water wave just 4 cm high.

The second type of pressure-coupled tsunami is driven by the AG waves. These "tsunami in the sky" comprise low-pressure, long-duration, dispersive, gravity-driven atmospheric wave trains that continuously impart energy to the ocean (*29*–*32*). Similar to the direct blast case, the atmosphere-ocean coupling of AG waves is rarely efficient because of the velocity differential between atmospheric waves (270 to 300 m/s) and typical tsunami waves (100 to 220 m/s). AG pressure waves decay more slowly with distance than blast pressures waves (~distance$^{-0.6}$ versus distance$^{-3/2}$), so they could be detected across the globe. Also of note is that atmospheric pressure waves can run over land, creating waves in isolated water bodies where normal tsunami would not reach. AG-coupled water waves, 5 to 10 cm high, thousands of kilometers away were reported to have arrived hours earlier than later "conventional" eruption-generated tsunami waves (movie S1) (*17*, *19*, *32*–*34*). These pressure-coupled tsunami are a curiosity but of no real near-field, local concern.

Lagging behind the HTHH pressure-coupled waves were the conventional tsunami generated by the explosive displacement of seawater. These travel on their own, guided by local $\sqrt{(g\,H)}$ speeds (*35*). Conventional tsunami were HTHH's primary destructive arm and the primary focus of our inquiry.

RESULTS

Yields and timing of the HTHH tsunamigenic blast sequence

By all accounts, the phreatoplinian HTHH eruption of 15 January 2022 involved a series of eruptive and explosive events that spanned hours (*7*, *36*). Eruptive events typically persist for several minutes, during which eruptive products are actively expelled from vents and great volcanic plumes are cast into the stratosphere (*37*, *38*). Explosive events, by contrast, constitute a large explosion of steam

Downloaded from https://www.science.org on April 14, 2023

generated by phreatomagmatic interactions [i.e., molten fuel coolant interactions (MFCI)]. MFCI explosions are sensed at distance as "sonic booms." Because they distort the entire atmospheric column, both eruptive and explosive events may be responsible for the widely documented AG waves (*9*–*14*, *16*, *17*, *33*). However, we contend that in the case of HTHH, the explosive or blast events created the bulk of tsunami (*28*, *34*).

While eruptive and explosive events go hand in hand in the HTHH sequence, the timings, spatial extent, and relative strengths of the two do not necessarily correlate well. In time, explosions last seconds, whereas eruptive events last minutes. In space, the loci of MFCI explosions need not necessarily be the same as the sites where eruptive products vented. Hence, the timing, spatial extent, and strength of the eruptive events deduced from satellite and ground observations (*8*, *15*, *16*, *39*–*42*) may not jive with those same features of explosive events extracted from tsunami data. Our goal is to develop a plausible time history of explosive events that explain 118 observed wave runup measurements and the two available tide gauge records in Nukuʻalofa, as illuminated by tsunami simulation. Ancillary information comes from eye- and earwitnesses, window breaking reports, and the barometric pressure gauge record from the Queen Salote Wharf in the port (Fig. 2A).

Earwitnesses in Nukuʻalofa (Fig. 1C) report hearing two blasts just before 4:00 UTC. Additional eyewitnesses report the first plumes rising from HTHH at 4:06 UTC, reaching an altitude >20 km by 4:11 UTC, and spreading umbrella-like over Nukuʻalofa by 4:25 UTC (*43*). We name these Blasts 1 and 2, but according to data recorded by the Nukuʻalofa tide gauges (Fig. 2B), they produced no meaningful tsunami. Two increasingly loud booms were heard within the next 30 min; we name these Blasts 3 and 4. Damaging tsunami waves from this pair most certainly struck Nukuʻalofaʻs west coast by 4:30 UTC and the waterfront of the city center by 4:36. The two tide-gauge records show the first wave arrival from Blast 3 at 4:26 (Fig. 2B). Tsunami simulation fixes wave travel time from the HTHH volcano to the Vuna and Queen Salote Wharfs at 18 and 20 min, respectively. As far as tsunami are concerned, Blast 3 must have occurred at 4:06 UTC. Given the precision of the gauge data and the certainty in the position of the Hunga caldera relative to the gauges, there is no wiggle room here. Furthermore, simulations show that a blast source at the volcano creates two or three separate arrivals at the tide gauges, separated by about 5 min (Fig. 2B). These later arrivals represent the rebound of the blast cavity. We interpret the first two peaks in the tide gauges as a record of Blast 3. About 12 min later, three or more excursions of up to 1.25 m are seen in both gauges. We interpret those as being sourced from larger Blast 4 at 4:18 UTC. Using blast scaling laws based on surface, free-air chemical and atomic explosions (*25*, *26*) and our concepts of blast-generated tsunami, we estimate the explosive yield of Blasts 3 and 4 at 0.5 and 4 Mt, respectively.

Although Blasts 3 and 4 as fixed above do an adequate job in matching the first 30 min of the tide gauge records, these two blast events alone are insufficiently powerful to reproduce the observed wave runup data. For a wide stretch along the north coast of Tongatapu waves ran up to 3 m above sea level (*28*), yet the tide gauges on the Queen Salote and Vuna Wharfs in Nukuʻalofa show excursions less than 1.25 m relative to current tide. Tide gauges often read low compared to runup because they measure only wave height (potential energy), while runup reflects both wave height and wave velocity (kinetic energy). In addition, both gauges are in compromised sheltered positions versus open coasts. Regardless, other widely spaced wave runup observations confirm that Blast 3 and 4 are lacking. A still bigger Blast 5 is needed.

The timing of Blast 5 is uncertain, but it can be bracketed. First, a weather station and communication tower situated on a 13-m-high ridge on western Tongatapu was toppled by Blast 5 tsunami (*44*). The station logged every 10 min but transmitted only on the hour. It last broadcasted at 5:00 UTC. Allowing 10 min of tsunami propagation delay from HTHH to the tower, fixes Blast 5 after 4:50 UTC. This timing is further confirmed by observations of people evacuating and later returning to the area (*44*). Second, and for reasons unknown, the tide gauge situated on Queen Salote Wharf stopped functioning at 5:24 UTC, a few minutes after the largest peak-to-peak value (>3 m) was recorded. The tide gauge on the Vuna Wharf, however, functioned throughout and recorded a third parcel of waves with peak-to-peak values >2.5 m starting at 5:15 UTC and persisting until at least 6:00 UTC. Allowing for wave propagation delays, we propose that Blast 5 at 4:56 UTC spawned these waves. It is tantalizing to think that Blast 5 waves themselves knocked the Queen Salote Wharf tide gauge out of commission, but this cannot be determined unequivocally.

How do we constrain the strength of Blast 5? There are at least two threads to pull here. One aspect is the reports of windows breaking in Nukuʻalofa. Breaking windows requires a quantifiable change in pressure, which, with overpressure versus distance formula (Eq. 3), constrains the explosive yield. In the 1960ʻs the Federal Aviation Authority collected a vast extent of sonic boom–related damage by flying supersonic jets over Oklahoma City six times a day for 26 weeks (*45*, *46*). Enough information was collected to construct probabilistic estimates of window glass breakage versus peak overpressure (Fig. 3A). Reading from those results, 5% of windows would break under an overpressure of 0.15 psi, and 30% would break under an overpressure of a 0.35 psi. Anecdotal reports from Nukuʻalofa suggest that 5 to 30% seems a reasonable span for glass breakage in the city. At 65-km distance, 0.15 and 0.35 psi correspond to explosive yields of 5 and 15 Mt, respectively (Fig. 3B). The barometric data recorded by the Tongan Met Office confirm that multiple pressure variations of up to 25 mbar (0.35 psi) occurred in the main city of Nukuʻalofa (65 km from HTHH; Fig. 2A). These signals, starting at 4:45, 4:58, and 5:44 UTC, associate with eruptive events as hot ash and gas were expelled from the caldera, resulting in long-period episodes of low pressure developing beneath the rising plume (Fig. 2A). Those signals are too long of period to break glass in themselves, but they do show that HTHH had the capacity to issue pressure variations strong enough to break glass. It is worth stating here that the pressure measurements in Fig. 2 are collected and averaged over 60-s intervals. Explosions related to glass-breaking pressure changes last just seconds and therefore become smoothed over or lost in the Nukuʻalofa barometer data.

The most direct thread to pull is the 118 wave runup height measurements that we have derived from fieldwork and analysis of time-separated remote sensing imagery and topography. After running a number of simulations, we fixed the 4:56 UTC Blast 5 at 15 Mt. This seemed to offer the most reasonable fit to all the anchored observations and collected measurements.

Downloaded from https://www.science.org on April 14, 2023

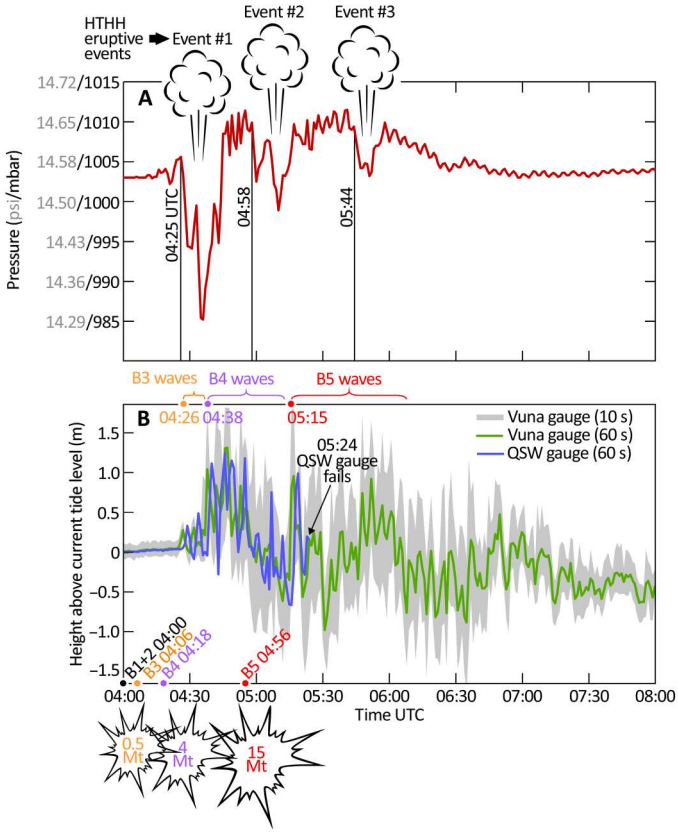

Fig. 2. Time-averaged surface station data recorded by the Tongan Met Office in the main port of Nukuʻalofa on 15 January 2022. (**A**) Barometric pressure records three long-period, low-pressure phases starting at 4:45, 4:58, and 5:44 UTC. We interpret these to be caused by the development of a low-pressure zone beneath the plume rising above HTHH. Averaged over 60 s. Intervals, these barometric data adequately capture these pressure drops that last approximately 20 min. Pressure anomalies generated by the tsunamigenic explosions are too short lived to be recorded. To time these explosions, we rely on ear- and eyewitness accounts and the signal of the arriving tsunami waves at the two Nukuʻalofa tide gauges. The tide data (**B**) come from two gauges, one on the Queen Salote Wharf (QSW) and the second 1.8 km away on the Vuna Wharf. Situated 65 km away, the waves spawned at HTHH take 20 min to transit to Nukuʻalofa. Two small blasts (Blasts 1 and 2) are reportedly heard in Nukuʻalofa at around 4:00 UTC, but these evidently do not generate tsunami. Earwitness accounts of blasts at 4:06 and 04:18 UTC correspond to parcels of waves arriving at the two tide gauges starting at 4:26 and 4:38, respectively. A third wave parcel is recorded arriving at 5:15 UTC, delivering the largest peak-to-peak variation in sea level (>3 m) recorded in the series, preempting the failure of the Queen Salote Wharf gauge at 5:24. We contend that this parcel was generated from Blast 5 at 4:56 UTC. The available data suggest that the explosive yields from Blasts 3, 4, and 5 were 0.5, 4, and 15 Mt, respectively.

Tsunami simulation

We simulated the tsunami parented by three explosive events of HTHH: Blast 3 at 4:06 UTC, Blast 4 at 4:18, and Blast 5 at 4:56 [Fig. 4, movie S2, and online material by Ward (*47*)]. Blast 3, the weakest of this trio, had a yield of 0.5 Mt. By 4:10 UTC (Fig. 4A), the waves spawned by it reached the 100-m isobath of the two carbonate platforms hosting the Tongatapu and Haʻapai island groups.

The 4:21 UTC time step (Fig. 4B) informs that Blast 3 waves reached the coastline of Tofua in the north and the west coast of Tongatapu in the south. At this early stage, simulated wave

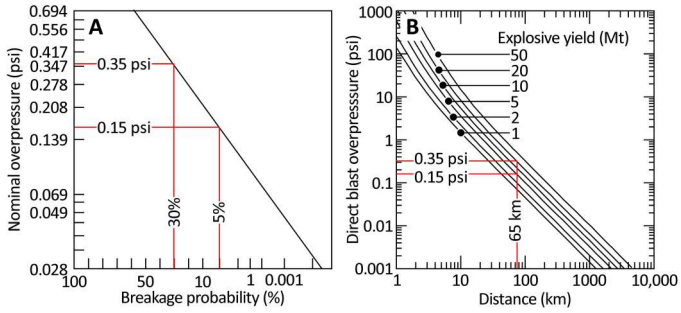

Fig. 3. Blast pressures, broken windows, and explosive yield. (**A**) In 1964, the U.S. Federal Aviation Authority (FAA) flew supersonic jet planes over Oklahoma City to evaluate the effect of sonic booms on people and property. From this exercise, the FAA developed probabilistic assessments of the likelihood of window glass breaking for a given overpressure (*46*). Witnesses report that the blast occurring shortly before 05:00 UTC broke windows in Nukuʻalofa, situated 65 km from the HTHH volcano. The FAA data instruct that overpressures of 0.35 and 0.15 psi would break between 30 and 5% of windows, a span that sensibly brackets the damage in Nukuʻalofa. Data formulated for overpressures at varying offset distance (Eq. 3) reveal that blasts with yields of 15 and 5 Mt, respectively, would deliver these pressures at 65 km (**B**).

runups are modest (<3 m). As Blast 3 waves reach Tofua and Tongatapu, the larger waves emanating from 4.0-Mt Blast 4 radiate away from HTHH, such that at 4:21 UTC, waves from both blasts are in play.

By 4:33 UTC (Fig. 4C), Blast 4 waves broadly impact all the islands in the model domain. Wave runups as high as 22 m are simulated to strike the southern coast of Tofua, while waves ranging from 3 to 13 m reach the western coast of Tongatapu. The main city of Nukuʻalofa, situated in a sheltered shallow lagoon on the northern coast of the island, has yet to experience meaningful waves. On this point, our simulation is in harmony with the data recorded by the tide gauges. These report sea-level perturbations of <0.5 m at 4:33 and must owe themselves to Blast 3. The western coastline of ʻEua has received wave runups of up to 8 m by 4:33 UTC, and all the western islands of the Haʻapai Group have been impacted by the Blast 4 waves, although the <3-m runups are small by comparison. The 4:33 UTC time step emphasizes the "wrap around" behavior of the waves in the south of the model domain. Note how the waves, initially radiating southward from HTHH, interact with the shallow bathymetry of Tongatapu and the complex of seamounts that lie 30 km to its west and shoal within 65 m of sea level (white box in Fig. 4C). These shallows refract the wavefronts to an easterly direction, a process reinforced by the presence of ʻEua Island, that ultimately succeeds in redirecting the southward travelling waves to a northerly path toward the eastern sides of the Tongatapu and Haʻapai platforms, albeit with waves greatly attenuated by this circuitous route.

By 5:00 UTC (Fig. 4D), 5 min after Blast 5 (15 Mt. at 4:56 UTC), its wavefront is already 30 km from HTHH and will imminently visit the western side of the Haʻapai platform.

By 5:14 UTC (Fig. 4E), the largest predicted wave runups (44.9 m) occur on the western coast of Tofua. Such extreme runups on Tofua are corroborated by scour marks observed on the flanks of this steep (and fortunately uninhabited) volcanic island, as corroborated by time-separated remote sensing, drone, and field observations (Figs. 5 to 7). By now, the many islands on the west side of the

Downloaded from https://www.science.org on April 14, 2023

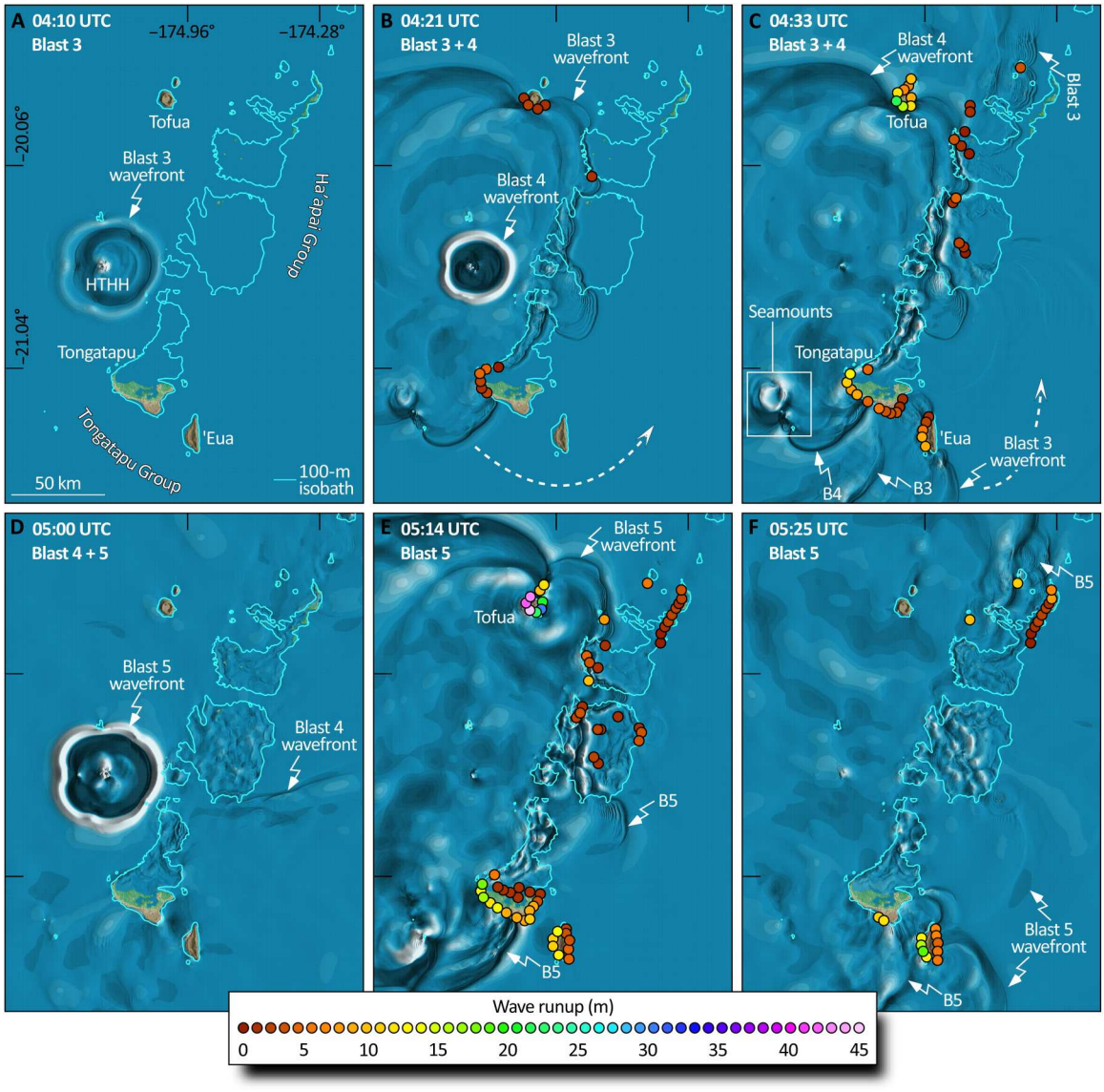

Fig. 4. Tsunami simulations for the repetitive blasts of HTHH. Wave propagation shown at T = 4:10 (**A**), 4:21 (**B**), 4:33 (**C**), 5:00 (**D**), 5:14 (**E**), and 5:25 UTC (**F**) and color scale depict maximum wave runup at the coast. These six time slices encompass the creation and propagation of waves from the three 15 January 2022 tsunamigenic explosions of HTHH. Highest runups in the model domain (45 m) are on the coastline of the northern island of Tofua that suffered the full unattenuated brunt of the tsunami. Receiving waves that have not crossed the shallow Tongatapu and Ha'apai carbonate platforms, the southwest coasts of the islands of Tongatapu and 'Eua also receive runups >15 m high. Most other island locations, being protected by fringing reefs and shallow lagoons, fare better. Note how Tongatapu and 'Eua refract waves from a southerly to a northerly path (e.g., broken white arrows on frames 4:21 and 4:33 UTC), thereby projecting tsunami onto the (sheltered) eastern flanks of the Tongatapu and Ha'apai platforms. Animation as movie S2.

Ha'apai platform receive Blast 5 waves, the largest impacts that these islands have so far suffered, but all <4 m high. Similarly, the west coasts of Tongatapu and 'Eua have by now received their largest wave runups, simulated to be 16 and 12 m for the two islands, respectively. The pair of tide gauges on the Nuku'alofa waterfront receive their largest peak-to-peak values at this time (>2.5 m; Fig. 8), while the simulation predicts similar wave runups of 1.5 to 2.5 m along the Nuku'alofa waterfront (Fig. 4E).

By 5:25 UTC (Fig. 4F), only the Blast 5 wavefront is active in the simulation. It has now transited the Ha'apai platform and swept the islands situated on its eastern flank (Ha'ano, Foa, Lifuka, Uoleva, and Uiha; Fig. 1 for locations). Between 2 and 8 m high, these runups are only marginally higher than those attributed to Blast 4. To the south, the Blast 5 wavefront has bent eastward around Tongatapu to impact 'Eua. Its west coast now receives the highest simulated runup at 17 m, just 1 m higher than the maximum achieved by smaller Blast 4. Notably, the Blast 5 wavefront, that has taken the faster, but longer, wrap around southerly route, now merges with waves from the same blast that traveled directly, but slowly, across the Ha'apai platform. The merged Blast 5 waves adopt the same northerly track, as those from Blasts 3 and 4 that

Downloaded from https://www.science.org on April 14, 2023

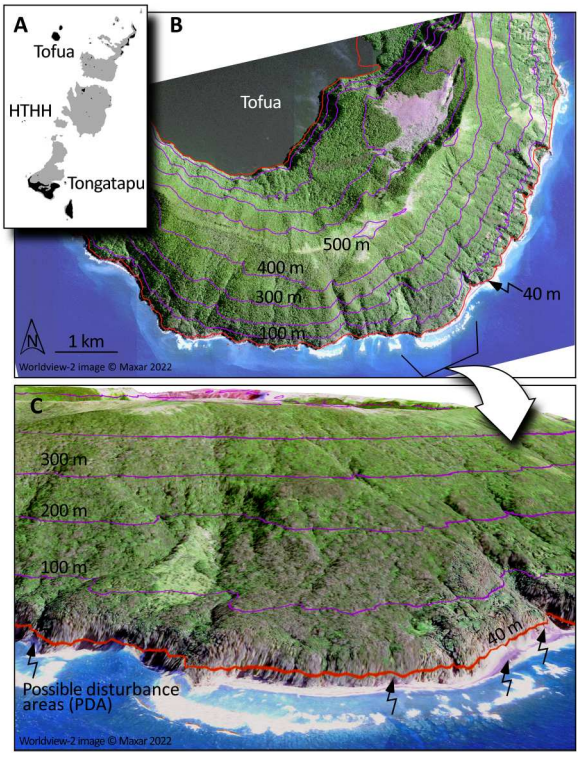

Fig. 5. Post-tsunami disturbances along the southern flank of Tofua Island based on synthetic aperture radar, DEM, and optical imaging analysis. (**A**) Location of Tofua 90 km north of the Hunga submarine caldera (HTHH). (**B**) Nadir view of the southern flanks of Tofua from Canadian Space Agency's (CSA) Radarsat Constellation Mission (RCM) C-band HH polarization spotlight SAR (1-m resolution, inverted in its backscatter) at 46° incidence with semitransparent Maxar WorldView (WV-02) visible wavelength data (resampled to 1 m) and superimposed DEM contours every 100 m from sea level (in purple), as well as the 40 m (above-sea-level) contour in orange. (**C**) Oblique view ray-traced using the co-registered synthetic aperture radar (SAR), with the 1-m ground sample distance (GSD) DEM, with the ocean view from WV-02 acquired 2 September 2022, and the inverted RCM-SAR acquired by the CSA in Spotlight (beam FSL30) mode on Aug. 24th, 2022. Pink to magenta correspond to possible disturbance areas (PDAs) identified in the satellite data. These putative tsunami-related disturbances require field validation for confirmation but are suggestive of runups up to 45 m in this steeply sloping region. GEDI and ICESat-2 LIDAR topography has been used to evaluate the steepest slopes in this central, southern portion of the Tofua volcanic island. RCM-SAR data courtesy of RCM image at 2022 courtesy of the government of Canada.

traveled 1 hour earlier are the last vestiges of the tsunami in the model domain.

Blast 5 offers an opportunity to examine the anatomy of the waves generated by a 15-Mt submarine volcanic explosion. Just 1 min after the detonation, the simulation shows the blast-coupled wave radiating symmetrically away from HTHH (Fig. 9A). This wave is already 20 km from HTHH by 4:57 UTC and travelling close to the speed of sound but only 28 cm high and decaying swiftly. Following behind is the conventional tsunami generated by the explosive displacement of seawater. Immediately after the explosion, the transient blast cavity that becomes the tsunami is 6 km across, forming a wave 85 m high on the north side of HTHH and 65 m high to the south (Fig. 9B). Although the blast is isotropic, the topography of the Hunga caldera is not. For this reason, the size of the conventional tsunami varies with azimuth.

Tracking the peak wave height of the Blast 5 tsunami as it reaches the shallows surrounding Tongatapu emphasizes the effectiveness of bathymetric attenuation (transect *X*-*X*′; Fig. 9B). Having travelled 55 km from HTHH, the 60-m wave that initially radiated south from the blast is 10 m high when it reaches the northern flank of the Tongatapu platform. As the wave crosses the fringing reef that veneers this flank, the height of the shoaling wave height nearly doubles (18 m). Then, because of breaking, the wave drops to only 3 m. Attenuation continues as the wave transits the 12 km of shallow water that extends out from the north coast of Tongatapu. The wave that eventually beaches on the island is <2 m high. By contrast, the Blast 5 wave that visits the south coast of Tongatapu, a portion of the island unprotected by shallow water, is 6× higher (12 m; Fig. 9B).

Last, as a reality check for the overall simulation, consider table S1, which lists the yield, energy release, and tsunami energy associated with Blasts 3, 4, and 5. At a minimum, for the calculation to be energetically acceptable, the energy of the tsunami produced must be less than the total energy lost in the blasts. Explosions in general are not very efficient sources of water waves because of the large proportion of energy lost to heat production, ejection of debris, turbulence, and seismic wave generation. Simulations here transfer just 5 to 7.5% of the energy toward tsunami generation. The calculations made for acceleration-capping steps detailed in Materials and Methods are energetically acceptable.

Accuracy of the tsunami simulation in space and time

We evaluated the performance of the simulation in space against 118 sites [Fig. 7 (A and B) for locations] distributed along 505 km of island coastline in the model domain (Fig. 7C). The performance of the simulation through time was judged from predicted and recorded water levels at the Queen Salote and Vuna Wharfs in the main city of Nuku'alofa (Fig. 8). At the 91 field-observed sites, simulated and measured runup heights are in good accordance, with a few notable exceptions.

For the Tongatapu Group and its surroundings, field measured runups measured at Fafa Island (site IDs 98 and 99; Fig. 7B) are up to 5 m higher than predicted by the simulation. In addition, for waves reaching the north coast of Tongatapu (sites 100 to 109), the simulated values are a bit low versus the field data. This underprediction intimates that the simulation overattenuates tsunami waves crossing the shallow shelf to the north of Tongatapu. In particular, the frictional coefficient c_d in Eq. 7 may be too large. On the west coast of Tongatapu, the situation reverses. Here, the simulation predicts higher wave runups than measured. Site IDs 44 through 55, for instance, show overpredictions up to 5 m in the extreme case (sites 49, 51, 53, and 54). Possibly, the simulated waves are insufficiently attenuated before impacting this coastline because of inadequate resolution of our near-shore bathymetry model. Note, though, that the west coast of Tongatapu experienced the largest waves in both the model and in reality. This deviation is acceptable considering the good agreement at all the other sites around the main island and adjacent 'Eua (sites 40 to 43).

For the Ha'apai Group, the simulation tends to underpredict field-measured wave heights on the central and east side of this platform by about 2.5 m (for instance, sites 13 to 36). On the west side of the Ha'apai Group, however, the simulation is in tune (e.g., sites 8 to 10). These facts again point toward an overattenuation in the

Downloaded from https://www.science.org on April 14, 2023

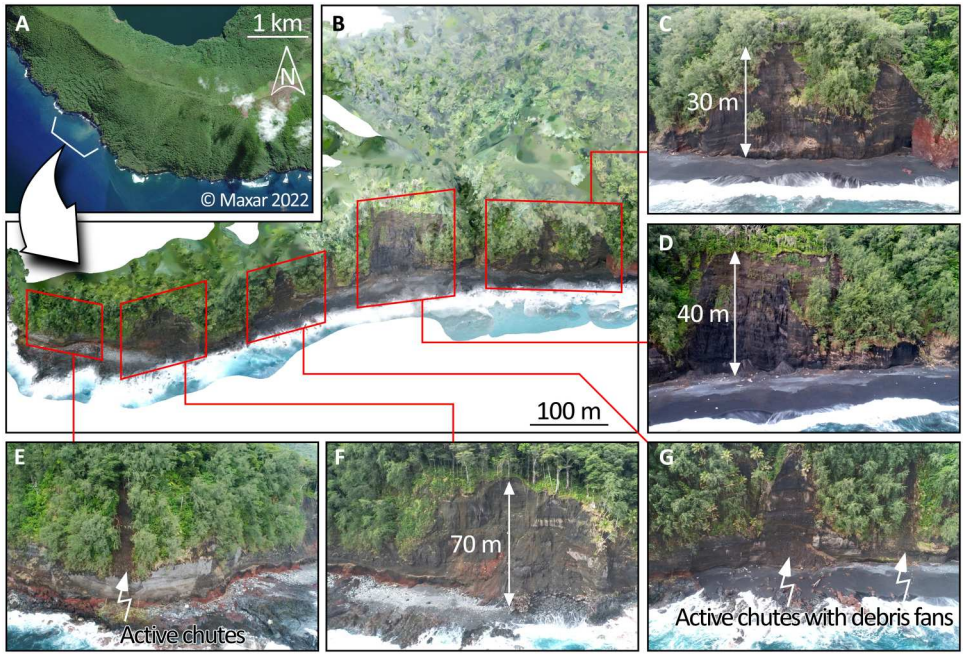

Fig. 6. Drone imaged post-tsunami disturbances along the south-southwest flank of Tofua Island. (**A**) Maxar Worldview-02 view of SSW Tofua, with arrow indicating the area of DJI drone imaging (14 October 2022). (**B**) Oblique ray-traced perspective view of the SSW flanks of Tofua developed from DJI drone data as a structure-from-motion DEM by NASA *Goddard*. Spatial resolution of this DEM is 8 cm, with ortho-image mosaic of drone images projected atop the topography. Of the 1500 m of coastline imaged, approximately 300 m show signs of recent disturbance (in the DEM), consistent with the anticipated impact of the 15 January 2022 megatsunami. Drone images (**C** to **F**) emphasize disturbances ranging in height from 30 to 70 m, including landslides (C, D, and D), fresh debris fans, and debris chutes with transported trees (E and G). DJI drone data were acquired by S.J.C.

simulation for waves crossing expanses of shallow water, west to east in this case.

We supplemented the 91 field-visited sites with an additional 27 sites where runups were derived from time-separated satellite and drone imagery with stereogrammetric topography and LIDAR. As detailed in Materials and Methods, observations from orbit are less precise than observations in the field and should be given less emphasis, yet satellite data provide calibration points in the remote locations unreachable during the field campaign. Satellite-derived runups around the Tongatapu Group accord well with the simulation (sites 77 to 83), reemphasizing the competence of the model in the south. Runups from satellite for the central and east side of the Haʻapai Group are higher than simulated, once more suggesting excessive shallow water attenuation (sites 29 to 31 and 34 to 39). For islands on the west side of the Haʻapai Group (sites 3 to 10), the simulation and the satellite measurements match. The highest runups, observed or simulated, are located on the steep coasts of Tofua Island. Here, the simulation predicts that the Blast 5 waves had runups that reached 25- to 30-m elevation on the Islandʻs southern coast (site 1) and 44 m on the west coast (site 2). Comparison of satellite and drone data before and after the HTHH eruption suggests vegetation scars at this height (Figs. 5 and 6). Although Tongatapu is closer to HTHH than Tofua (65 versus 90 km), the south coast of Tofua is unique in the model domain in not being mantled by a fringing reef or situated atop a shallow carbonate platform. Incoming tsunami would not be attenuated before running up the steep sides of this still-active volcanic island. Remote and surrounded by sea cliffs, Tofua is a national park and uninhabited. The high runups on Tofua radically contrast those on the other islands that average <5 m. Further reconnaissance of Tofua in the aftermath of the 2022 tsunami is warranted using field and additional LIDAR-based methods, given its uniqueness.

Simulation performance in time between 4:15 and 6:00 UTC, was assessed against the data collected by the Queen Salote and Vuna Wharfs tide gauges, both situated in Nukuʻalofa on the north side of the main island of Tongatapu. The main channel of the Vuna Wharf gauge delivers data averaged over 60 s. Additional data streams deliver maximum and minimum water levels at 10-s intervals. These provide estimates of peak-to-peak variations (Fig. 8A). The tide gauge on the Queen Salote Wharf (Fig. 8B) lacks the 10-s data stream, but it did deliver data averaged over 60 s. until the instrument failed at 5:24 UTC.

Note that the two records correlate well in time, with waves arriving at Vuna Wharf 2 min earlier than at Queen Salote Wharf. The former is approximately 2 km closer to HTHH than the latter. The simulation correctly captures this 2-min offset. The simulation reveals that the first two or three observed wave peaks originate from Blast 3 starting at 04:26 UTC followed by two or three Blast 4 waves starting at 4:38 UTC. These gradually decline until 5:15 UTC, when the largest peak-to-peak deviations are seen in both the simulation and gauge data. These mark the arrival of Blast 5 waves. Only in this period (5:15 to 5:35 UTC) of maximum commotion induced by the Blast 5 waves do the gauge and the simulation diverge. The simulation predicted water levels up to 1.5 m higher than recorded at the Vuna Wharf. By 5:40 UTC, the predicted Blast 5 waves realign with the gauge record. The limited data from the Queen Salote Wharf gauge provides further confirmation. Again, the successive increase in peak-to-peak deviation of sea level

Downloaded from https://www.science.org on April 14, 2023

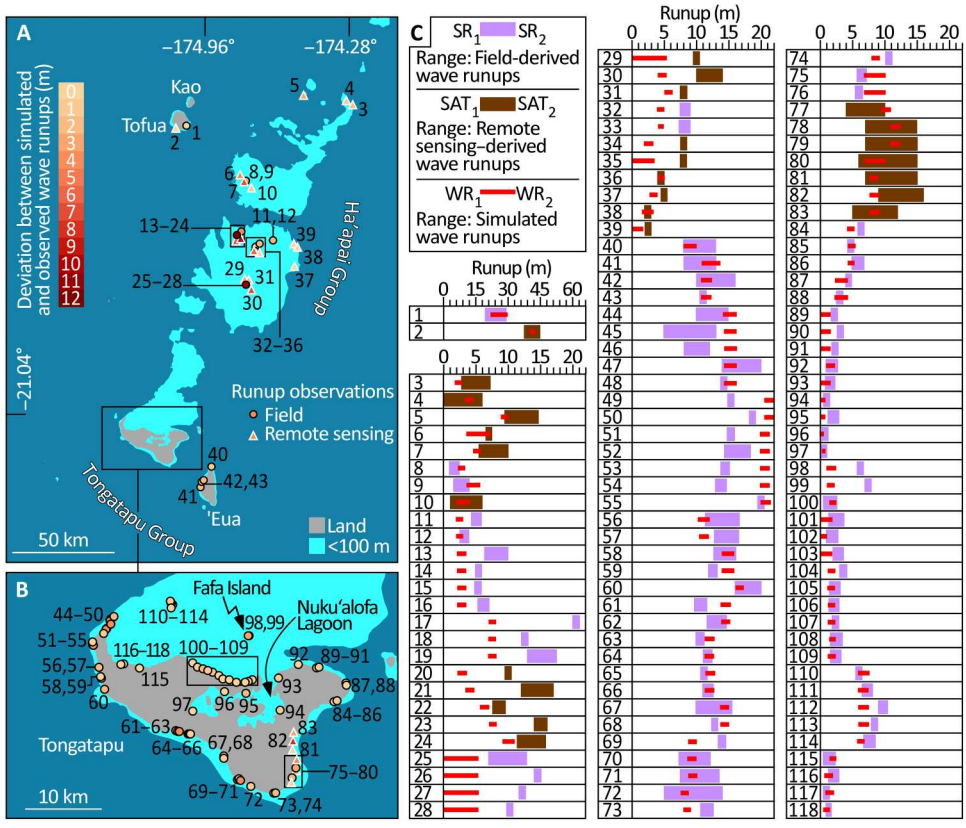

Fig. 7. Comparison of simulated and observed wave runups at 118 sites. ID numbers relate the sites mapped in (**A**) and (**B**) to the comparisons of observed versus simulated data graphed in (**C**). In the maps, sites where runups were observed in the field are depicted by circles, and those observed using time-separated remote sensing are triangles. These symbols are color-coded to depict the discrepancy between observed runups and those predicted by tsunami simulation. In (C), purple and brown bars represent runup observations made in the field and made using remote sensing, respectively. Runups from the tsunami simulation are red bars. In each case, the bars span two estimates of observed and simulated runup at each site (Materials and Methods for details).

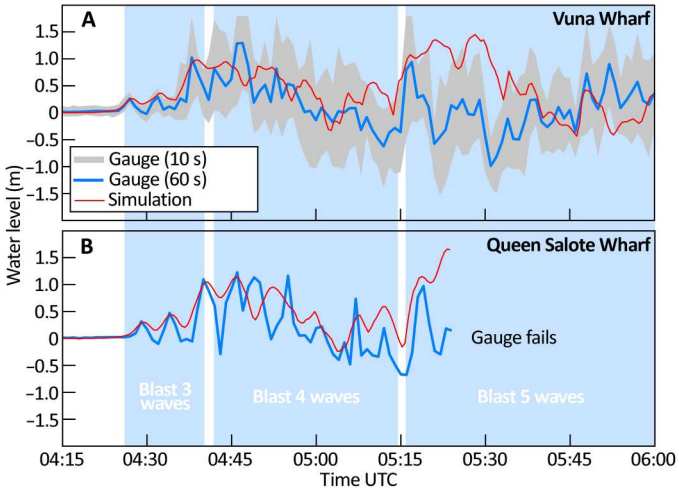

Fig. 8. Comparison of simulated and observed water levels. Sea level data taken from Vuna Wharf (**A**) and Queen Salote Wharf (**B**) in the Nuku'alofa Lagoon (Tongatapu). The tidal signal has been removed and the current tide level set to 0 m at 4:15 UTC. Simulated water levels (red lines) mimic the gauge data through the passage of the Blast 3 and 4 waves, but slightly deviate for the period 5:15 to 5:35 UTC following the arrival of the Blast 5 waves, before falling back into step by 5:40 UTC.

induced by Blast 3 and Blast 4 waves is captured, as is their gradual dissipation. You can see a hint of Blast 5 waves arrive at the Queen Salote Wharf at 5:17 UTC, shortly before the station went offline.

The tide gauge records and the field-measured runups reveal a conflict. The former show peak offsets <1.25 m, while all the field-measured runups in the area (sites 100 to 109) fall in the range of 2 to 3 m. As suggested above, tide gauges often read low compared to runup because they measure only wave height (potential energy), while runup reflects both wave height and wave velocity (kinetic energy). Still, the simulation cannot match both. It compromised by slightly unpredicting the field-measured sites and slightly over-predicting the tide gauges between 5:15 and 5:35 UTC.

DISCUSSION

Planetary-wide observations of long-period atmospheric disturbances that emanated from the HTHH eruption (VEI = 6.3) have delivered a good understanding of the volcano's eruptive sequence (*9*–*15*, *17*, *18*). By contrast, the blasts embedded in that sequence and the tsunami that they spawned are poorly constrained. Unlike whole atmosphere disturbances, direct blast pressures and extreme tsunami waves cannot be observed at distance. Public-domain, near-field data recorded from Tonga are scant. We rely on recordings from one barometric station and two tide gauges on

Downloaded from https://www.science.org on April 14, 2023

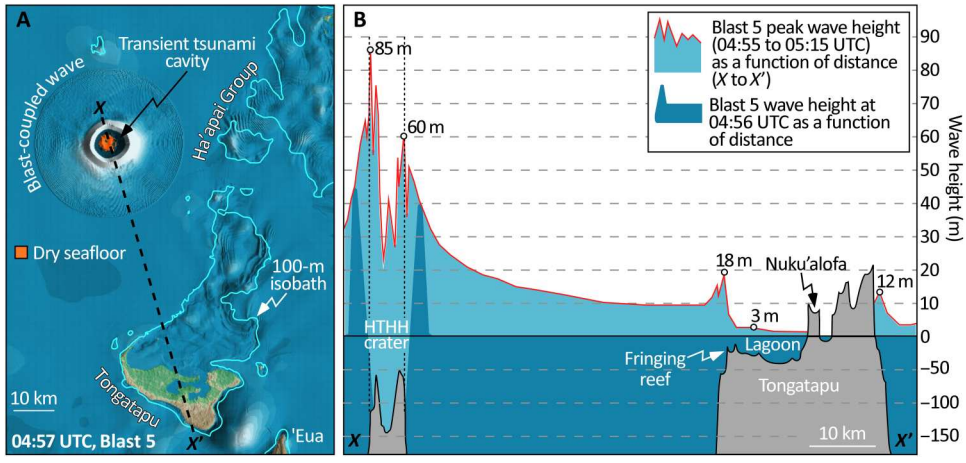

Fig. 9. Blast-coupled waves and conventional tsunami issued from HTHH. (**A**) Catches the simulation at 04:57 UTC, 1 min after Blast 5. Travelling close to the speed of sound, the tiny blast-coupled water wave is now 20 km from HTHH. Following behind is the conventional tsunami generated by the explosive displacement of seawater. Note how the 15-Mt blast is sufficient to expose dry seafloor (orange). This "bottoming out" diminishes the efficiency of tsunami generation. The *X* to *X*′ transect delivers the cross section through the simulation shown in (**B**). Here, the red line charts the simulated peak wave height during the time that Blast 5 was active (4:56 to 5:15 UTC). Note that the height of the conventional tsunami as it departs the HTHH crater varies from 85 m in the north to 60 m in the south. Note too how the tsunami interacts with the shallow Tongatapu platform. The wave crossing the fringing reef outboard Tongatapu Island is 18 m high but is efficiently attenuated to only 3 m as it enters the broad lagoon behind the reef. Waves that eventually beach on the north coast of Tongatapu are <2 m high. Unprotected by a fringing reef, the wave visited upon the south coast of Tongatapu is 12 m high.

Tongatapu, situated 65 km from HTHH. These data come with limitations. The barometric data average over 60-s intervals, too long to capture short-duration (a few seconds) blast pressure variations. The tide gauge data also average over 60 s and record activity at sheltered locations in Nuku′alofa Lagoon. Waves there probably underrepresent free-field sea-level motions (*48*). Still, by casting a wide net, we can fix times and yields of the blasts that generated tsunami. This relies on several threads: (i) the booms heard by earwitnesses in Nuku′alofa; (ii) reports there of breaking windows; (iii) relationships between applied pressure and window breakage established by the U.S. Federal Aviation Authority (FAA); (iv) the tide gauge records; (v) runup values from widely ranged field, drone, and satellite measurements; and (vi) the fact that the blasts were surface, open-air explosions, as quantified by Eq. 3.

Taking the data as a basket, we argue a sequence of three blasts. The first at 4:06 UTC with a yield of 0.5 Mt, the second at 4:18 UTC with 4 Mt, and the third at 4:56 UTC with a yield of 15 Mt. We recognize that many mechanisms during a volcanic eruption generate water waves (*3*, *27*). Likely, to some extent, many of these were in play during the HTHH sequence. Still, we demonstrate that three isotropic explosive wave sources adequately explain the existing tsunami data without recourse to other more complex mechanisms. Furthermore, we stress again that blast events differ from eruptive events and their timings may differ. For instance Wright *et al.* (*16*) interpret the Nuku′alofa barometric data to place events at 4:36, 5:10, 5:51, and 8:46 UTC (their extended data figure 8). We interpret these several 20-min-long, low-pressure signals to represent eruptive phases of the volcano, not explosive phases. The latter are too short lived to be recorded in that data. Furthermore, the timings from the work of Wright *et al.* (*16*) cannot be reconciled with the arrival times of tsunami waves along the Nuku′alofa waterfront, as reported by eyewitnesses and recorded by tide gauges there. Observations of AG modes, not tsunami, are central to the work of Wright *et al.* (*16*), so the different interpretations are understandable. However, it is relevant to note that our estimate of 15 Mt for 4:56 UTC Blast 5 is bracketed by the 9 to 37 Mt derived by Astafyeva *et al.* (*40*) from ionosphere perturbations for the combined yield from the explosive and eruptive episodes of HTHH, although lower than the 25 Mt estimated by Pakoksung *et al.* (*28*) in their near-field tsunami model.

The timing of largest tsunami waves witnessed during the volcano′s activity, the toppling of the weather station on western Tongatapu (*44*), and the tide gauge excursions (Fig. 2), all fix Blast 5 to 4:56 UTC. Curious that the largest explosive event of the sequence falls nearly one-half hour after the largest eruptive events, which occurred between 4:15 and 4:30 UTC (*9*, *12*, *13*, *37*). Curious too is that the largest explosive event of the sequence has a negligible expression in the global teleseismic records (*12*, *13*, *41*, *42*). Perhaps Blast 5 was not the same phreatomagmatic explosion-driven detonation as Blasts 3 and 4? Maybe part of Blast 5′s 15 Mt of tsunami-generating energy came from non-explosive sources? A sudden structural collapse of the eruption column followed by submarine pyroclastic density currents could be sufficiently tsunamigenic to explain the data, while being less likely to be recorded seismically. It is up to other researchers to explore the plausibility of this.

Another explanation might be that near–ocean surface phreatomagmatic explosions such as Blast 5 (and Blasts 3 and 4 for that matter) simply do not couple well to the solid Earth and thus do not show strong seismic signals. Instead, these types of explosions may send much of their energy upward or transfer a large proportion into tsunami or hydro-acoustic waves.

The third explanation as to why Blast 5 failed to register in the far-field records is that we may have overestimated its yield. Two possibilities exist here. First, multibeam sonar bathymetric mapping in 2015 and again in 2016 revealed the Hunga caldera (with HTHH on its NW rim) to have a mean water depth of ~150 m across its entire floor (*49*, *50*). Surveys following the 2022 eruption reveal the caldera to languish >1000 m below sea level

Downloaded from https://www.science.org on April 14, 2023

(Shane Cronin, pers. comm., 16 January 2023). It is logical to assume that Blasts 3, 4, and 5 were issued over ever-increasing water depth as the caldera collapsed. Our simulation fixed water depth at the volcano of about 150 m and Blast 5 tsunami "bottomed out" (Fig. 9), thus limiting its size. If, at the time of Blast 5, deeper water existed there, such "bottoming out" may not have occurred and a smaller yield would be needed to make the same-size tsunami. The second possibility for overestimating the yield of Blast 5 is that it was not a surface, open-air explosion to which Eq. 3 applies. An explosion deeper in the water column, for instance, might be more efficient than the surface explosions of Blasts 3 and 4. That is, the yield needed to produce a given overpressure and tsunami size might be less for Blast 5 than Eq. 3 suggests.

An intriguing finding from the simulation is the effect of blast yield on wave height at various locations. Consider the animation of our simulation (Supplementary Material) and the time steps extracted from it (Fig. 4). Tsunami that traveled an unhindered path impinged on islands with wave heights that correlate to blast yield. At 65-km distance, for instance, the west coast of Tongatapu receives wave runups of 8 to 12 m from 4-Mt Blast 4 but 15 to 17 m waves from 15-Mt Blast 5. Runups on the south coast of Tofua, 90 km from HTHH, are 17 to 23 m high from Blast 4 and 30 to 45 m from Blast 5. These results suggest that tripling blast yield approximately doubles the size of the tsunami unattenuated by a fringing reef. For many islands atop the Tongatapu and Ha′apai platforms, however, waves extensively attenuate as they cross expansive shallow water (e.g., Fig. 9B). After this journey, blast yield and wave height apparently decouple. Ha′ano, Foa, Lifuka, Uolva, and Uiha (Fig. 1B) mantle the southeastern flank of the Ha′apai platform. By the time the waves have traversed 30 to 50 km of platform to Uiha, for instance, Blast 4 and 5 wave runups are nearly identical (runups average 2 to 4 m) despite Blast 5 being >3× larger. Because shallow water attenuation is proportional to wave height squared (Eq. 7), larger-in does not mean larger-out.

The simulation also highlights the diversity of wave heights across short distances. On the main island of Tongatapu, Blast 5 waves beach on the southern coastline up to 17 m. Just a few kilometers to the southeast, the simulation predicts heights of only 10 m (Fig. 4E), and 10 km to the east, the Nuku′alofa tide gauges record only 1.5-m waves. On Eua, average wave height on the west coast is 15 m but only 5 m on the east coast, 7 km away. Similarly, satellite and drone imaging of Tofua (Figs. 5 and 6) show substantial variability of disturbance along the mapped coastlines, suggesting that tsunami risk varies on short length scales.

Also captured in the simulation is how each blast makes more than one wave. The first wave associates with the direct outward push of the blast. Later ones associate with the rebound and oscillation of the blast cavity and span several minutes (*28*). Remaining separate when crossing deep water, these waves interact once impeded by bathymetry. Rising to within 65 m of sea level, a complex of seamounts lies 30 km off the west coast of Tongatapu (labeled in Fig. 4C). Here, multiple Blast 5 waves coalesce as the leading front stalls over this topography. The seamounts then act like secondary point sources of waves. Susceptible to bathymetry, waves spawned by the blasts refract as they pass the aforementioned seamounts and bend around the south coast of Tongatapu. The topography conspires to redirect the southward travelling wavefronts onto a northerly path, ultimately leading the tsunami to wrap around the Tongatapu platform to the point where even the sheltered eastern side of the Ha′apai platform is illuminated. Another way that waves reach the east side of the Ha′apai platform is via the more direct (but slower) route across the platform top. With sequential wavefronts emanating from the successive HTHH explosions but traversing the archipelago via different routes at different speeds, Blast 4 and Blast 5 waves interact in the west of the model domain, although the former generated 40 min earlier. These results highlight how a single tsunami can remain "captured" by an archipelago, how waves from multiple blasts interact even when separated by hours, and how wrap-around behavior can result in sizable tsunami beaching in areas where they would not necessarily be expected.

The 15 January 2022 eruption of HTHH (within the submarine Hunga caldera) holds lessons for both past and future tsunamigenic events along the Tonga-Kermadec arc. Tonga makes a compelling case study, as substantial evidence exists for tsunami inundating large areas of Tongatapu in precolonial history (*3*, *4*). Considering sedimentological and archaeological evidence, Lavigne *et al.* (*3*) pin a major tsunami in the mid-15th century with runup heights up to 30 m. The powerful Tu′i Tonga kingdom that then existed was severely affected, and an oral history remains more than 500 years later. We believe the 2022 HTHH tsunami to be of similar scale. Simulated and field-measured wave runups on the west coast of Tongatapu approach 20 m. On the western coast of Tofua, they are over 40 m. Our simulated peak height of the Blast 5 wave at HTHH was 85 m (Fig. 9), in good accordance with the 90 m predicted by Heidarzadeh *et al.* (*34*). Fortunately, the urban center of Tonga, Nuku′alofa, situates in a sheltered lagoon. Had the population been dispersed along the exposed ocean-facing coastlines of the archipelago, a much higher death toll might be anticipated than the estimated six lives lost.

The wave runups from the 2022 HTHH explosive event comfortably meet the criteria for a megatsunami and contend for the largest event anywhere in the past 100 years. For comparison, field records of the 1883 Krakatau (Indonesia) and 2011 Tohoku (Japan) tsunamis both indicate wave heights of 35 to 40 m (*51*–*53*), placing these events and HTHH in a similar league. The tsunami spawned by the 2018 eruption of the Anak Krakatoa produced maximum wave runups of "only" 13 m (but killed 437 people) (*54*–*56*). Another megatsunami generated by the 1957 Andreanof Islands earthquake in Alaska (*57*) had wave runups in the range of 9 to 23 m (*58*), about half the maximum of HTHH. Likely the deadliest in recorded history, the 2004 Sumatra tsunami produced wave runups generally less than 10 m (*59*) and locally up to 20 m (*60*), killing 227,898 people in 14 countries (*61*).

With once-in-a-century wave runups, some exceeding 40 m, the death toll from HTHH would be expected to be far greater. The main factors that led to this, we suggest, are the quirk of the location, a worldwide pandemic, and increased evaluation drills and awareness efforts carried out in the years prior. The western coastlines of Tongatapu, where wave runups locally exceeded 15 m, are rugged, exposed, and mantled by sea cliffs. Only a handful of tourist resorts are located there, and these were closed because of the coronavirus disease 2019 (COVID-19) pandemic. Similarly, the west coast of ′Eua is sparsely populated, limiting human exposure to the 10- to 12-m waves that beached there. The coast of Tofua is entirely uninhabited and rimmed by the highest sea cliffs in the archipelago. The main settlements in all of Tonga safely face Nuku′alofa Lagoon, the best possible scenario to duck the full brunt of a megatsunami. The

Downloaded from https://www.science.org on April 14, 2023

many other inhabited islands in the archipelago sit atop the Ha′apai platform, also providing ample shallow water to attenuate the tsunami to beach with heights <5 m. Again, geography was kind. No inhabited islands situate on the western flank of the Ha′apai platform where the tsunami were at their fiercest. The normally busy resort islands of Ha′ano, Foa, Lifuka, Uolva, and Uiha sit on the sheltered eastern flank of the Ha′apai platform. In a lucky twist, these resorts were shuttered because of COVID-19.

Disaster management policies and preparation also contributed to the low death toll. After the 2004 Indian Ocean tsunami, coastal nations worldwide became more risk alert. The Government of Tonga held their first kingdom-wide tsunami evacuation drill in November 2017 and performed a comprehensive multidisaster risk assessment survey a mere 7 months before the 2022 event. These activities, as well as the Polynesian islander′s connection with their geoheritage (*62*), are credited as a major component of the unexpectedly low number of casualties. The outcomes from the HTHH event provide an ideal example of how such efforts are critical to mitigate tsunami disaster impacts and to reducing the death toll.

Most volcanically generated megatsunami can only be studied through geological or archeological evidence, wherein much of the evidence is erased or altered over time. Two well-known examples are the 1883 eruption of Krakatoa, wherein 36,000 lives were lost (*63*) and the ~1600 BCE Theran eruption in Santorini, wherein the death toll is highly speculative given that only one human victim has been reported within well-constrained tsunami deposits (*64*). Both of these events share similar multiple eruption sequences similar to observations from HTHH (e.g., four modeled for Thera and four described for Krakatoa). HTHH provides the opportunity to observe at scale and in real time through data collected at tide and barometric gauges and in the immediate aftermath, providing the parameters to better understand those previous events, as well as contribute to future disaster preparations.

MATERIALS AND METHODS

Topo-bathymetry models

Key to our tsunami simulation is an accurate topo-bathymetric surface. For water depths >25 m, we assembled Global Multi-Resolution Topography, a global multibeam compilation (*65*) with a spatial resolution of 100 m. Shallower than 25 m, we used the spectrally derived bathymetry of Purkis *et al.* (*20*) that uses the depth-derivation algorithm of Kerr and Purkis (*66*) to deliver a spatial resolution of 5 m and is calibrated by abundant sonar soundings from the field.

Coarse-resolution terrestrial DEMs for all islands in the model domain were provided by the NASADEM (*67*) built from the ASTER Global Digital Elevation Map (ASTER-GDEM v.3) derived from stereo-pairs of satellite scenes from the ASTER archive at 30-m spatial resolution (*68*) combined with the Shuttle Radar Topography Mission (SRTM) measurements. Building forward from the work of Garvin *et al.* (*50*), we mapped those islands around which wave runup heights were harvested, using a combination of 1- to 3-m compact polarimetric Radarsat Constellation Mission (RCM) Spotlight C-band SAR (synthetic aperture radar) and stereo-pairs of 0.5-m panchromatic Maxar WorldView data (WV-02). These terrain models were validated against GEDI (*69*) and ICESat-2 satellite LIDAR.

Tsunami simulation

In the absence of added frictions, the Tsunami Squares method accelerates fixed squares of fluid at each time step by

$$\frac{D\mathbf{v}(\mathbf{r},t)}{Dt} = -g\nabla\eta(\mathbf{r},t) - \frac{\nabla P(\mathbf{r},t)}{\rho_w} \quad (2)$$

v is fluid velocity (m/s). $-g\,\nabla\,\eta(\mathbf{r}, t)$ is the acceleration due to gravity g (m/s^2), working on the slope of the water surface $\nabla\eta(\mathbf{r}, t)$, and $-\nabla P(\mathbf{r}, t)/\rho_w$ is the acceleration due to the gradient of explosive overpressure versus time, $P(\mathbf{r}, t)$, where P is applied overpressure pressure (Pa) and ρ_w is fluid density (kg/m^3). Data from surface, open-air atomic bomb tests (*25*) fix the decay of peak overpressure with distance r as

$$P(r) = 98.368\left[\frac{W}{r^3}\right] + 42.644\left[\frac{W}{r^3}\right]^{\frac{1}{2}} \quad (3)$$

Peak overpressure, P, is pounds per square inch (psi = 6895 Pa). r is the distance from the blast in kilometers, and W is the explosive yield in megatons (1000 kg) of trinitrotoluene (TNT). $P(\mathbf{r}, t)$ then becomes a function of distance only

$$P(\mathbf{r},t) = P(r,t) = P(r)F(W,r,t) \quad (4)$$

where $F(W, r, t)$ is a unitless normalized time history of pressure that we take as a simple exponential

$$\mathrm{F}(W,r,t) = e^{-[t-t_0\,(r)]/\Delta(W,r)}\;\; t > t_0\;(r) \quad (5)$$

In Eq. 5, $t_0(r)$ is the arrival time of the blast at distance r; that is, distance in kilometers divided by the speed of sound, 0.34 km/s. The decay constant Δ depends on yield and peak overpressure by

$$\Delta(W,r) = 4\;\max\;[W^{1/3}, 3.87\;W^{1/3}/P^{1/2}(r)] \quad (6)$$

Units in Eq. 6 are Δ (in seconds), W (in megatons) and P (in psi). Equation 5 is only slightly modified from the work of Newmark (*26*). Because peak overpressure (Eq. 3) goes to infinity as r goes to zero, $-\nabla P(\mathbf{r}, t)/\rho_w$ in Eq. 2 has to be capped somehow. We choose to limit this term to the acceleration due to gravity g. This restriction affects only the first few seconds of the blast.

Last, to account for frictional losses in water <30 m deep, an additional acceleration is added to Eq. 2

$$\frac{D\mathbf{v}(\mathbf{r},t)}{Dt} = -g\nabla\eta(\mathbf{r},t) - \frac{\nabla P(\mathbf{r},t)}{\rho_w} - \frac{c_\mathrm{d}\,|\mathbf{v}(\mathbf{r},t)|\mathbf{v}(\mathbf{r},t)}{H(\mathbf{r})} \quad (7)$$

where $H(\mathbf{r})$ is water depth and c_d is a unitless friction coefficient. The simulations used squares of 200-m size and were time stepped by 1 s. The behavior of breaking waves and bore formation are implicitly captured in the nonlinear formulation of Tsunami Squares.

Validation of the tsunami simulation

We audited our tsunami simulation across space and through time. For the former, we compared simulated versus observed wave runups at 118 coastal sites. To assess performance through time, we compared water levels recorded by the Queen Salote and Vuna Wharf tide gauges on the Nuku′alofa waterfront (Tongatapu) with simulated water levels for the duration of the HTHH explosive episodes.

Downloaded from https://www.science.org on April 14, 2023

Of the 118 validation sites, 91 were visited in the 3 months following the 15 January 2022 HTHH eruption, allowing direct measurement of wave runups above the tidal stage at the time of the tsunami (*44*). On the basis of sedimentary deposits, erratic clasts, floated pumice, and damaged vegetation and infrastructure, two wave runup heights (SR_1 and SR_2) were determined for each site (fig. S1). These measurements do not represent minimum and maximum runup values but rather give a range of potential variability. We also extracted two runup values from the tsunami simulation; WR_1 represents the maximum height above sea level where flow depth goes to zero (akin to field-measured SR_1), and WR_2 is like the field-measured SR_2.

At a further 27 sites, we assembled pre- and post-tsunami satellite imagery and estimated runups based on the topography to which vegetation had been felled after 15 January 2022. Where cloud-free satellite imagery existed before and after the tsunami, Maxar WV-02 and WV-03 satellite data were used (Fig. 10). These satellites produce images in eight multispectral bands with pixel dimensions of 0.5 m by 0.5 m once sharpened using the broadband panchromatic channel. In the rare cases where either the "pre" or "post" WorldView optical images were too cloudy, Canadian Space Agency's (CSA) RCM-SAR scenes served as replacement (Fig. 5). These have pixel dimensions of 1 m by 3 m in the spotlight-imaging beam mode (FSL30 at ~45° incidence). Such SAR imaging data are uncompromised by clouds and microwave backscatter (*70*) and easily discern felled vegetation, as well as disturbances related to slopes or changes of meter-scale surface texture. In addition, satellite LIDAR measurements of tree heights on the southern flanks of Tofua from ISS/GEDI (*69*) illustrated canopy heights in potentially disturbed areas ranging from 5-m to over 45-m elevation above sea level, with a typical value of about 20 m, consistent with highly approximated tree size measurements from submeter scale WV images. The 1.5-km section of the south-southwest coastline of Tofua where the wave runups were simulated to be at their highest was additionally surveyed using a DJI drone. This survey delivered a DEM with 8-cm resolution and oblique images showing disturbances to the flanks of the island varying from 30 to 70 m elevation (Fig. 6). Comparison to pansharpened WV-02/03 images acquired before 15 January 2022 indicate these disturbances to postdate the tsunami. For all wave runups derived from remote sensing data, we adapted the workflows of Purkis *et al.* (*71*) and Wu *et al.* (*72*) and digitized the most seaward position of standing vegetation in the pre-tsunami image for each site and then repeated this exercise for the post-tsunami imagery. We fixed wave runup values equal to the highest elevation (as audited from the RCM-SAR images and Maxar WorldView DEMs) of vegetation standing before 15 January but knocked down in the post-tsunami imagery. To estimate variability, we sampled 5-m intervals along 200-m coastline transects and noted similar heights. The 10th and 90th percentile of these values form SAT_1 and SAT_2, respectively.

While a valuable supplement to the field data, estimating wave runups from satellite comes with two caveats. First, the spatial resolution of the satellite data limits the fidelity to which coastal change can be detected, often because of challenging viewing geometry or illumination constraints. Damage to coastal vegetation or deposition of erratic clasts at a scale finer than the pixel size of the satellite imaging will be missed or ambiguously depicted. Second, minor damage to vegetation that might be obvious in the field, is unlikely to be detected from orbit, except in special cases via LIDARs such as GEDI, or ICESat-2 (which directly measure vegetation structure). In this respect, we consider the 27 satellite-derived runup heights to be conservative compared to the 91 field-measured heights.

Last, to assess the accuracy of the simulation through time, we compared water levels recorded at the Queen Salote and Vuna Wharfs tide gauges with the levels predicted by the tsunami simulation. Water levels recorded by the two gauges were detrended to remove the tidal signal such that the water level was at 0-m elevation at 4:15 UTC. The comparison between the two tide gauges and the

Downloaded from https://www.science.org on April 14, 2023

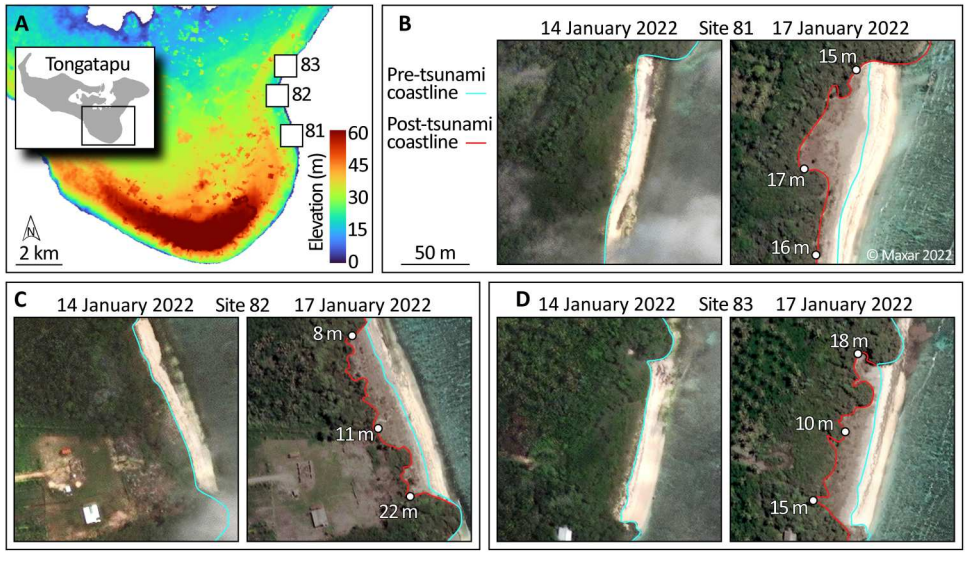

Fig. 10. Pre- and post-tsunami vegetation damage on Tongatapu. (**A**) Location of three examples from southeastern Tongatapu (site IDs 81, 82, and 83) where downed coastal vegetation allows wave runup heights to be estimated from a DEM built from stereo-pairs of WorldView satellite data. (**B**), (**C**), and (**D**) compare the position of the vegetated coastline in pre- (14 January 2022) and post-tsunami (17 January) WorldView imagery for these sites and spot measurements of wave runup from the DEM.

simulation spans the interval 04:15 UTC to 6:00 UTC; the Queen Salote Wharf gauge failed at 5:24 UTC.

Supplementary Materials

This PDF file includes:
Fig. S1
Table S1
Legends for movie S1 and S2

Other Supplementary Material for this manuscript includes the following:
Movies S1 and S2

REFERENCES AND NOTES

1. C. Timm, D. Bassett, I. J. Graham, M. I. Leybourne, C. E. J. de Ronde, J. Woodhead, D. Layton-Matthews, A. B. Watts, Louisville seamount subduction and its implication on mantle flow beneath the central Tonga–Kermadec arc. *Nat. Commun.* **4**, 1720 (2013).
2. I. E. M. Smith, R. C. Price, The Tonga–Kermadec arc and Havre–Lau back-arc system: their role in the development of tectonic and magmatic models for the western Pacific. *J. Volcanol. Geotherm. Res.* **156**, 315–331 (2006).
3. F. Lavigne, J. Morin, P. Wassmer, O. Weller, T. Kula, A. V. Maea, K. Kelfoun, F. Mokadem, R. Paris, M. N. Malawani, A. Faral, M. Benbakkar, S. S. Copard, C. M. Vidal, T. Tu'I'afitu, F. Kitekei'aho, M. Trautmann, C. Gomez, Bridging legends and science: field evidence of a large tsunami that affected the Kingdom of Tonga in the 15th Century. *Front. Earth Sci.* 9, 10.3389/feart.2021.748755, (2021).
4. C. Frohlich, M. J. Hornbach, F. W. Taylor, C. C. Shen, 'A. Moala, A. E. Morton, J. Kruger, Huge erratic boulders in Tonga deposited by a prehistoric tsunami. *Geology* **37**, 131–134 (2009).
5. M. Colombier, B. Scheu, F. B. Wadsworth, S. Cronin, J. Vasseur, K. J. Dobson, K. U. Hess, M. Tost, T. I. Yilmaz, C. Cimarelli, M. Brenna, B. Ruthensteiner, D. B. Dingwell, Vesiculation and quenching during surtseyan Eruptions at Hunga Tonga-Hunga Ha'apai Volcano, Tonga. *J. Geophys. Res. Solid Earth* **123**, 3762–3779 (2018).
6. M. Brenna, S. J. Cronin, I. E. M. Smith, A. Pontesilli, M. Tost, S. Barker, S. Tonga'onevai, T. Kula, R. Vaiomounga, Post-caldera volcanism reveals shallow priming of an intra-ocean arc andesitic caldera: Hunga volcano, Tonga. *Lithos* **412**, 106614 (2022).
7. S. Self, R. S. J. Sparks, Characteristics of widespread pyroclastic deposits formed by the interaction of silicic magma and water. *Bull. Volcanol.* **41**, 196–212 (1978).
8. J. Thurin, C. Tape, R. Modrak, Multi-event explosive seismic source for the 2022 M_w 6.3 Hunga Tonga submarine volcanic *Eruption. Record* **2**, 217–226 (2022).
9. A. Amores, S. Monserrat, M. Marcos, D. Argüeso, J. Villalonga, G. Jordà, D. Gomis, Numerical simulation of atmospheric Lamb waves generated by the 2022 Hunga-Tonga volcanic eruption. *Geophys. Res. Lett.* **49**, e2022GL098240 (2022).
10. J.-T. Lin, P. K. Rajesh, C. C. H. Lin, M.-Y. Chou, J.-Y. Liu, J. Yue, T.-Y. Hsiao, H.-F. Tsai, H.-M. Chao, M.-M. Kung, Rapid conjugate appearance of the giant ionospheric Lamb wave signatures in the northern hemisphere after Hunga-Tonga volcano eruptions. *Geophys. Res. Lett.* **49**, e2022GL098222 (2022).
11. D. Adam, Tonga volcano eruption created puzzling ripples in Earth's atmosphere. *Nature* **601**, 497 (2022).
12. R. S. Matoza, D. Fee, J. D. Assink, A. M. Iezzi, D. N. Green, K. Kim, L. Toney, T. Lecocq, S. Krishnamoorthy, J.-M. Lalande, K. Nishida, K. L. Gee, M. M. Haney, H. D. Ortiz, Q. Brissaud, L. Martire, L. Rolland, P. Vergados, A. Nippress, J. Park, S. Shani-Kadmiel, A. Witsil, S. Arrowsmith, C. Caudron, S. Watada, A. B. Perttu, B. Taisne, P. Mialle, A. L. Pichon, J. Vergoz, P. Hupe, P. S. Blom, R. Waxler, S. De Angelis, J. B. Snively, A. T. Ringler, R. E. Anthony, A. D. Jolly, G. Kilgour, G. Averbuch, M. Ripepe, M. Ichihara, A. Arciniega-Ceballos, E. Astafyeva, L. Ceranna, S. Cevuard, I.-Y. Che, R. De Negri, C. W. Ebeling, L. G. Evers, L. E. Franco-Marin, T. B. Gabrielson, K. Hafner, R. G. Harrison, A. Komjathy, G. Lacanna, J. Lyons, K. A. Macpherson, E. Marchetti, K. F. M. Kee, R. J. Mellors, G. Mendo-Pérez, T. D. Mikesell, E. Munaibari, M. Oyola-Merced, I. Park, C. Pilger, C. Ramos, M. C. Ruiz, R. Sabatini, H. F. Schwaiger, D. Tailpied, C. Talmadge, J. Vidot, J. Webster, D. C. Wilson, Atmospheric waves and global seismoacoustic observations of the January 2022 Hunga eruption, Tonga. *Science* **377**, 95–100 (2022).
13. D. A. Yuen, M. A. Scruggs, F. J. Spera, Y. Zheng, H. Hu, S. R. Mc Nutt, G. Thompson, K. Mandli, B. R. Keller, S. S. Wei, Z. Peng, Z. Zhou, F. Mulargia, Y. Tanioka, Under the surface: Pressure-induced planetary-scale waves, volcanic lightning, and gaseous clouds caused by the submarine eruption of Hunga Tonga-Hunga Ha'apai volcano. *Earthquake Res. Adv.* **2**, 100134 (2022).
14. S. N. Kulichkov, I. P. Chunchuzov, O. E. Popov, G. I. Gorchakov, A. A. Mishenin, V. G. Perepelkin, G. A. Bush, A. I. Skorokhod, Y. A. Vinogradov, E. G. Semutnikova, J. Šepic, I. P. Medvedev, R. A. Gushchin, V. M. Kopeikin, I. B. Belikov, D. P. Gubanova, A. V. Karpov, A. V. Tikhonov, Acoustic-gravity Lamb waves from the eruption of the Hunga-Tonga-Hunga-Hapai volcano, its energy release and impact on aerosol concentrations and tsunami. *Pure Appl. Geophys.* **179**, 1533–1548 (2022).
15. D. R. Themens, C. Watson, N. Žagar, S. Vasylkevych, S. Elvidge, A. M. Caffrey, P. Prikryl, B. Reid, A. Wood, P. T. Jayachandran, Global propagation of ionospheric disturbances associated with the 2022 Tonga Volcanic Eruption. *Geophys. Res. Lett.* **49**, e2022GL098158 (2022).
16. C. J. Wright, N. P. Hindley, M. J. Alexander, M. Barlow, L. Hoffmann, C. N. Mitchell, F. Prata, M. Bouillon, J. Carstens, C. Clerbaux, S. M. Osprey, N. Powell, C. E. Randall, J. Yue, Surface-to-space atmospheric waves from Hunga Tonga-Hunga Ha'apai eruption. *Nature* **609**, 741–746 (2022).
17. T. Kubota, T. Saito, K. Nishida, Global fast-traveling tsunamis driven by atmospheric Lamb waves on the 2022 Tonga eruption. *Science* **377**, 91–94 (2022).
18. M. T. Ramírez-Herrera, O. Coca, V. Vargas-Espinosa, Tsunami effects on the coast of Mexico by the Hunga Tonga-Hunga Ha'apai volcano eruption, Tonga. *Pure Appl. Geophys.* **179**, 1117–1137 (2022).
19. P. Lynett, M. McCann, Z. Zhou, W. Renteria, J. Borrero, D. Greer, O. Fa'anunu, C. Bosserelle, B. Jaffe, S. P. la Selle, A. Ritchie, A. Snyder, B. Nasr, J. Bott, N. Graehl, C. Synolakis, B. Ebrahimi, G. E. Cinar, Diverse tsunamigenesis triggered by the Hunga Tonga-Hunga Ha'apai eruption. *Nature* **609**, 728–733 (2022).
20. S. J. Purkis, A. C. R. Gleason, C. R. Purkis, A. C. Dempsey, P. G. Renaud, M. Faisal, S. Saul, J. M. Kerr, High-resolution habitat and bathymetry maps for 65,000 sq. km of Earth's remotest coral reefs. *Coral Reefs* **38**, 467–488 (2019).
21. J. Wang, S. N. Ward, L. Xiao, Numerical modelling of rapid, flow-like landslides across 3-D terrains: A Tsunami Squares approach to El Picacho landslide, El Salvador, September 19, 1982. *Geophys. J. Int.* **201**, 1534–1544 (2015).
22. L. Xiao, S. N. Ward, J. Wang, Tsunami squares approach to landslide-generated waves: application to Gongjiafang Landslide, Three Gorges Reservoir, China. *Pure Appl. Geophys.* **172**, 3639–3654 (2015).
23. J. Wang, S. N. Ward, L. Xiao, Tsunami Squares modelling of the 2015 June 24 Hongyanzi landslide generated river tsunami in Three Gorges Reservoir, China. *Geophys. J. Int.* **216**, 287–295 (2019).
24. S. J. Purkis, S. Ward, H. Shernisky, G. Chimienti, A. Sharifi, F. Marchese, F. Benzoni, M. Rodrigue, M. E. Raymo, A. Abdulla, Tsunamigenic potential of an incipient submarine landslide in the Tiran Straits. *Geophys. Res. Lett.* **49**, e2021GL097493 (2022).
25. N. Newmark, R. Hansen, Design of blast resistant structures. *Shock and Vibration Handbook* **3**, 1–19 (1961).
26. N. Newmark, External blast in *Proceedings of the International Conference on the Planning and Design of Tall Buildings* (Lehigh University, 1972), vol. 1b, pp. 661–676.
27. R. Paris, A. D. Switzer, M. Belousova, A. Belousov, B. Ontowirjo, P. L. Whelley, M. Ulvrova, Volcanic tsunami: A review of source mechanisms, past events and hazards in Southeast Asia (Indonesia, Philippines, Papua New Guinea). *Nat. Hazards* **70**, 447–470 (2014).
28. K. Pakoksung, A. Suppasri, F. Imamura, The near-field tsunami generated by the 15 January 2022 eruption of the Hunga Tonga-Hunga Ha'apai volcano and its impact on Tongatapu. *Sci. Rep.* **12**, 15187 (2022).
29. H. Kanamori, J. Mori, D. G. Harkrider, Excitation of atmospheric oscillations by volcanic eruptions. *J. Geophys. Res. Solid Earth* **99**, 21947–21961 (1994).
30. F. Press, D. Harkrider, Air-sea waves from the explosion of Krakatoa. *Science* **154**, 1325–1327 (1966).
31. D. Harkrider, F. Press, The Krakatoa air—sea waves: An example of pulse propagation in coupled systems. *Geophys. J. Int.* **13**, 149–159 (1967).
32. R. Omira, R. S. Ramalho, J. Kim, P. J. González, U. Kadri, J. M. Miranda, F. Carrilho, M. A. Baptista, Global Tonga tsunami explained by a fast-moving atmospheric source. *Nature* **609**, 734–740 (2022).
33. M. Carvajal, I. Sepúlveda, A. Gubler, R. Garreaud, Worldwide signature of the 2022 Tonga volcanic tsunami. *Geophys. Res. Lett.* **49**, e2022GL098153 (2022).
34. M. Heidarzadeh, A. R. Gusman, T. Ishibe, R. Sabeti, J. Šepić, Estimating the eruption-induced water displacement source of the 15 January 2022 Tonga volcanic tsunami from tsunami spectra and numerical modelling. *Ocean Eng.* **261**, 112165 (2022).
35. M. W. Hayward, C. N. Whittaker, E. M. Lane, W. L. Power, S. Popinet, J. D. L. White, Multilayer modelling of waves generated by explosive subaqueous volcanism. *Nat. Hazards Earth Syst. Sci.* **22**, 617–637 (2022).
36. Y. Zheng, H. Hu, F. Spera, M. Scruggs, G. Thompson, Y. Jin, T. Lapen, S. M. Nutt, K. Mandli, Z. Peng, D. Yuen, Episodic magma hammers in the recent cataclysmic eruption of Hunga Tonga-Hunga Ha'apai. *Research Square (Preprint)* , (2022).

Downloaded from https://www.science.org on April 14, 2023

37. J. L. Carr, Á. Horváth, D. L. Wu, M. D. Friberg, Stereo plume height and motion retrievals for the record-setting Hunga Tonga-Hunga Ha'apai eruption of 15 January 2022. *Geophys. Res. Lett.* **49**, e2022GL098131 (2022).
38. S. R. Proud, A. T. Prata, S. Schmauß, The January 2022 eruption of Hunga Tonga-Hunga Ha'apai volcano reached the mesosphere. *Science* **378**, 554–557 (2022).
39. B. J. Harding, Y.-J. J. Wu, P. Alken, Y. Yamazaki, C. C. Triplett, T. J. Immel, L. C. Gasque, S. B. Mende, C. Xiong, Impacts of the January 2022 Tonga volcanic eruption on the ionospheric dynamo: ICON-MIGHTI and swarm observations of extreme neutral winds and currents. *Geophys. Res. Lett.* **49**, e2022GL098577 (2022).
40. E. Astafyeva, B. Maletckii, T. D. Mikesell, E. Munaibari, M. Ravanelli, P. Coisson, F. Manta, L. Rolland, The 15 January 2022 Hunga Tonga eruption history as inferred from ionospheric observations. *Geophys. Res. Lett.* **49**, e2022GL098827 (2022).
41. R. Garza-Girón, T. Lay, F. Pollitz, H. Kanamori, L. Rivera, Solid Earth-atmosphere interaction forces during the 15 January 2022 Tonga eruption. *Sci. Adv.* **9**, eadd4931 (2023).
42. R. J. Le Bras, M. Zampolli, D. Metz, G. Haralabus, P. Bittner, M. Villarroel, H. Matsumoto, G. Graham, N. M. Özel, The Hunga Tonga–Hunga Ha'apai Eruption of 15 January 2022: Observations on the International Monitoring System (IMS) hydroacoustic stations and synergy with seismic and infrasound sensors. *Seismol. Res. Lett.* **94**, 578–588 (2023).
43. M. Delmar, Extended Footage - Tongas Jan. 15th Volcanic Eruption Hunga Tonga Hunga Ha'apai as seen from the ground. *YouTube Video from* https://www.youtube.com/watch?v=3US-AxvGfE4 (2022) [accessed throughout 2022].
44. J. C. Borrero, J. Cronin, F. H. Latu'ila, P. Tukuafu, N. Heni, A. M. Tupou, T. Kula, O. Fa'anunu, C. Bosserelle, E. Lane, P. Lynett, L. Kong, Tsunami runup and inundation in Tonga from the January 2022 eruption of Hunga Volcano. *Pure Appl. Geophys.* **180**, 1–22 (2022).
45. P. N. Borsky, "Community reactions to sonic booms in the Oklahoma City area. Volume 2. Data on community reactions and interpretations," (National Opinion Research Center New York, 1965).
46. D. A. Hilton, V. Huckel, D. J. Maglieri, R. Steiner, "Sonic-boom exposures during FAA community response studies over a 6-month period in the Oklahoma City area" (1964).
47. S. N. Ward, Hunga Tonga Tsunami. *YouTube Video from* https://www.youtube.com/watch?v=3Ms1yjO23VI (2022) [accessed throughout 2022].
48. P. L. Liu, Damping of water waves over porous bed. *J. Hydraul. Div.* **99**, 2263–2271 (1973).
49. S. Cronin, M. Brenna, I. Smith, S. Barker, M. Tost, M. Ford, S. Tonga'onevai, T. Kula, R. Vaiomounga, New volcanic island unveils explosive past. *Eos, Transactions American Geophysical Union* **98**, 18–23 (2017).
50. J. B. Garvin, D. A. Slayback, V. Ferrini, J. Frawley, C. Giguere, G. R. Asrar, K. Andersen, Monitoring and modeling the rapid evolution of Earth's newest volcanic island: *Hunga Tonga Hunga Ha'apai* (Tonga) using high spatial resolution satellite observations. *Geophys. Res. Lett.* **45**, 3445–3452 (2018).
51. E. Pelinovsky, B. H. Choi, A. Stromkov, I. Didenkulova, H.-S. Kim, in *Tsunamis: Case Studies and Recent Developments,* K. Satake, Ed. (Springer, 2005), pp. 57–77.
52. N. Mori, T. Takahashi, T. Yasuda, H. Yanagisawa, Survey of 2011 Tohoku earthquake tsunami inundation and run-up. *Geophys. Res. Lett.* 38, 10.1029/2011GL049210, (2011).
53. N. Mori, T. Takahashi; The 2011 Tohoku Earthquake Tsunami Joint Survey Group, Nationwide post event survey and analysis of the 2011 Tohoku earthquake tsunami. *Coastal Engineering Journal* **54**, 1250001–1250027 (2012).
54. M. Heidarzadeh, T. Ishibe, O. Sandanbata, A. Muhari, A. B. Wijanarto, Numerical modeling of the subaerial landslide source of the 22 December 2018 Anak Krakatoa volcanic tsunami, Indonesia. *Ocean Eng.* **195**, 106733 (2020)
55. T. Zengaffinen, F. Løvholt, G. K. Pedersen, A. Muhari, Modelling 2018 Anak Krakatoa flank collapse and tsunami: Effect of landslide failure mechanism and dynamics on tsunami generation. *Pure Appl. Geophys.* **177**, 2493–2516 (2020).
56. P. S. Putra, A. Aswan, K. A. Maryunani, E. Yulianto, S. H. Nugroho, V. Setiawan, Post-event field survey of the 22 December 2018 Anak Krakatau tsunami. *Pure Appl. Geophys.* **177**, 2477–2492 (2020).
57. R. C. Witter, G. A. Carver, R. W. Briggs, G. Gelfenbaum, R. D. Koehler, S. P. la Selle, A. M. Bender, S. E. Engelhart, E. Hemphill-Haley, T. D. Hill, Unusually large tsunamis frequent a currently creeping part of the Aleutian megathrust. *Geophys. Res. Lett.* **43**, 76–84 (2016).
58. D. Nicolsky, J. Freymueller, R. C. Witter, E. Suleimani, R. Koehler, Evidence for shallow megathrust slip across the Unalaska seismic gap during the great 1957 Andreanof Islands earthquake, eastern Aleutian Islands, Alaska. *Geophys. Res. Lett.* **43**, 10,328–310,337 (2016).
59. B. H. Choi, S. J. Hong, E. Pelinovsky, Distribution of runup heights of the December 26, 2004 tsunami in the Indian Ocean. *Geophys. Res. Lett.* 33, 10.1029/2006GL025867, (2006).
60. J. C. Borrero, C. E. Synolakis, H. Fritz, Northern Sumatra field survey after the December 2004 great Sumatra earthquake and Indian Ocean tsunami. *Earthq. Spectra* **22**, 93–104 (2006).
61. UNESCO-IOC, International Tsunami Information Center (ITIC). http://itic.ioc-unesco.org/index.php, (2021).
62. K. Németh, Geoheritage and geodiversity aspects of catastrophic volcanic eruptions: Lessons from the 15th of January 2022 Hunga Tonga - Hunga Ha'apai eruption, SW Pacific. *Int. J. Geoheritage Parks* **10**, 546–568 (2022).
63. B. H. Choi, E. Pelinovsky, K. Kim, J. Lee, Simulation of the trans-oceanic tsunami propagation due to the 1883 Krakatau volcanic eruption. *Nat. Hazards and Earth Syst. Sci.* **3**, 321–332 (2003).
64. V. Şahoğlu, J. H. Sterba, T. Katz, Ü. Çayır, Ü. Gündoğan, N. Tyuleneva, İ. Tuğcu, M. Bichler, H. Erkanal, B. N. Goodman-Tchernov, Volcanic ash, victims, and tsunami debris from the Late Bronze Age Thera eruption discovered at Çeşme-Bağlararası (Turkey). *Proc. Natl. Acad. Sci. U.S.A.* **119**, e2114213118 (2022).
65. W. B. Ryan, S. M. Carbotte, J. O. Coplan, S. O'Hara, A. Melkonian, R. Arko, R. A. Weissel, V. Ferrini, A. Goodwillie, F. Nitsche, J. Bonczkowski, R. Zemsky, Global multi-resolution topography synthesis. *Geochem. Geophys. Geosyst.* 10, 10.1029/2008GC002332, (2009).
66. J. M. Kerr, S. Purkis, An algorithm for optically-deriving water depth from multispectral imagery in coral reef landscapes in the absence of ground-truth data. *Remote Sens. Environ.* **210**, 307–324 (2018).
67. R. Crippen, S. Buckley, P. Agram, E. Belz, E. Gurrola, S. Hensley, M. Kobrick, M. Lavalle, J. Martin, M. Neumann, Q. Nyugen, P. Rosen, J. Shimada, M. Simard, W. Tung, NASADEM global elevation model: Methods and progress. ISPRS International Archives of the Photogrammetry, Remote Sensing and Spatial Information Sciences, Vol. XLI-B4, 2016, pp.125–128.
68. M. Abrams, R. Crippen, H. Fujisada, ASTER global digital elevation model (GDEM) and ASTER global water body dataset (ASTWBD). *Remote Sens. (Basel)* **12**, 1156 (2020).
69. R. Dubayah, J. Armston, S. P. Healey, J. M. Bruening, P. L. Patterson, J. R. Kellner, L. Duncanson, S. Saarela, G. Ståhl, Z. Yang, H. Tang, J. B. Blair, L. Fatoyinbo, S. Goetz, S. Hancock, M. Hansen, M. Hofton, G. Hurtt, S. Luthcke, GEDI launches a new era of biomass inference from space. *Environ. Res. Lett.* **17**, 095001 (2022).
70. D. Huntley, D. Rotheram-Clarke, A. Pon, A. Tomaszewicz, J. Leighton, R. Cocking, J. Joseph, Benchmarked RADARSAT-2, SENTINEL-1 and RADARSAT Constellation Mission Change-Detection Monitoring at North Slide, Thompson River Valley, British Columbia: ensuring a Landslide-Resilient National Railway Network. *Can. J. Remote Sens.* **47**, 635–656 (2021).
71. S. J. Purkis, R. Gardiner, M. W. Johnston, C. R. C. Sheppard, A half-century of coastline change in Diego Garcia – The largest atoll island in the Chagos. *Geomorphology* **261**, 282–298 (2016).
72. M. Wu, V. K. Duvat, S. J. Purkis, Multi-decadal atoll-island dynamics in the Indian Ocean Chagos Archipelago. *Glob. Planet. Change* **202**, 103519 (2021).

Acknowledgments: We are grateful for productive discussions with S. Day, E. Geist, P. McGillivary, and V. Chirayath. We are indebted to the crew of the M/Y Golden Shadow, through the generosity of HRH Prince Khaled bin Sultan, for inexhaustible help during our 2013 field campaign in Tonga. NASA roles in this work were supported by the RRNES-06 investigation at the NASA Goddard Space Flight Center, courtesy of G. Bawden and J. Kaye, with help from the GEDI Science Team (Blair, Hofton, and Luthcke). CSA RCM radar data were provided via J.B.G.'s special vetted user status (NASA), with thanks to the Government of Canada (C. Giguere, E. Albrecht, and their colleagues at CSA). S.J.C. acknowledges funding support from the University of Auckland, and the New Zealand Ministry of Business, Innovation and Employment, Endeavour Fund Project UOAX1913. S.J.C. thanks members of the Tongan Navy and the Tongan Geoscience Services (especially T. Kula and F. Latu'ila) for logistical and field assistance during data acquisition, as well as R. Palu from Pacific Sunrise Fishing Ltd. We further thank two anonymous reviewers for their constructive critique of this manuscript. Any use of trade, firm, or product names is for descriptive purposes only and does not imply endorsement by the U.S. Government. **Author contributions:** S.J.P. and S.N.W. conceived the study and led the analysis and write-up. The Tsunami Squares model was run by S.N.W. Remote sensing predicated on NASA and CSA products was directed by J.B.G. and D.S., while M.P.-L. assembled WorldView data. S.J.C. ideated and conducted all fieldwork. N.M.F. completed the change detection from WorldView data and developed the bathymetric grid for the simulation, assisted by A.D. **Competing interests:** The authors declare that they have no competing interests. **Data and materials availability:** All data needed to evaluate the conclusions in the paper are present in the paper and/or the Supplementary Materials.

Submitted 3 November 2022
Accepted 9 March 2023
Published 14 April 2023
10.1126/sciadv.adf5493

Downloaded from https://www.science.org on April 14, 2023

ScienceAdvances

The 2022 Hunga-Tonga megatsunami: Near-field simulation of a once-in-a-century event

Sam J. Purkis, Steven N. Ward, Nathan M. Fitzpatrick, James B. Garvin, Dan Slayback, Shane J. Cronin, Monica Palaseanu-Lovejoy, and Alexandra Dempsey

Sci. Adv., **9** (15), eadf5493.
DOI: 10.1126/sciadv.adf5493

View the article online
https://www.science.org/doi/10.1126/sciadv.adf5493
Permissions
https://www.science.org/help/reprints-and-permissions

Downloaded from https://www.science.org on April 14, 2023

Use of this article is subject to the Terms of service

Science Advances (ISSN) is published by the American Association for the Advancement of Science. 1200 New York Avenue NW, Washington, DC 20005. The title *Science Advances* is a registered trademark of AAAS.
Copyright © 2023 The Authors, some rights reserved; exclusive licensee American Association for the Advancement of Science. No claim to original U.S. Government Works. Distributed under a Creative Commons Attribution NonCommercial License 4.0 (CC BY-NC).